

Microtomographic PIV measurements of viscoelastic instabilities in a 3D micro-contraction

Daniel W. Carlson, Amy Q. Shen, and Simon J. Haward[†]

Micro/Bio/Nanofluidics Unit, Okinawa Institute of Science and Technology Graduate University, Onna, Okinawa 904-0495, Japan.

(Received xx; revised xx; accepted xx)

Viscoelastic flow through an abrupt planar contraction geometry above a certain Weissenberg number (Wi) is well known to become unstable upstream of the contraction plane via a central jet separating from the walls and forming vortices in the salient corners. Here, for the first time we consider three-dimensional (3D) viscoelastic contraction flows in a microfabricated glass square-square contraction geometry. We employ state-of-the-art microtomographic particle image velocimetry to produce time-resolved and volumetric quantification of the 3D viscoelastic instabilities arising in a dilute polymer solution driven through the geometry over a wide range of Wi but at negligible Reynolds number. Based on our observations, we describe new insights into the growth, propagation, and transient dynamics of an elastic vortex formed upstream of the 3D micro-contraction due to flow jetting towards the contraction. At low Wi we observe vortex growth for increasing Wi , followed by a previously unreported vortex growth plateau region. In the plateau region, the vortex circulates around the jet with a period that decreases with Wi but an amplitude that is independent of Wi . In addition, we report new out-of-plane asymmetric jetting behaviour with a phase-wise dependence on Wi . Finally, we resolve the rate-of-strain tensor \mathbf{D} and ascribe local gradients in \mathbf{D} as the underlying driver of circulation via strain-hardening of the fluid in the wake of the jet.

Key words:

1. Introduction

Entry flow has historically received attention as a canonical case for non-Newtonian fluid dynamics (Boger (1987); White *et al.* (1987)), and as a benchmark for developing computational models capable of studying highly elastic flows (Afonso *et al.* (2011); Pimenta & Alves (2017)). Under negligible inertia (i.e., Reynolds numbers $Re \ll 1$), for Weissenberg numbers ($Wi = \lambda \dot{\gamma}$, where λ is the fluid relaxation time and $\dot{\gamma}$ the shear rate) beyond a critical value $Wi_c \approx 0.5$, pipe flow moving towards a contraction becomes sufficiently elastic that it separates from the upstream walls, forming a central ‘jet’ that enters the constriction and vortices around the mouth of the constriction (McKinley *et al.* (1991); Rothstein & McKinley (1999)). Initially the corner vortices are static in their placement as Wi is increased, but eventually grow in size until a Hopf bifurcation characterized by a periodic fluctuation of the vortex separation point occurs. For $Wi > Wi_p \gg Wi_c$, the vortices become increasingly unsteady for increasing Wi (McKinley *et al.* (1991); Rothstein & McKinley (1999, 2001)), and may lead to a period-doubling route to chaos (McKinley *et al.* (1991)). The onset and subsequent dynamics of this elastic flow instability are highly sensitive to the

[†] Email address for correspondence: simon.haward@oist.jp

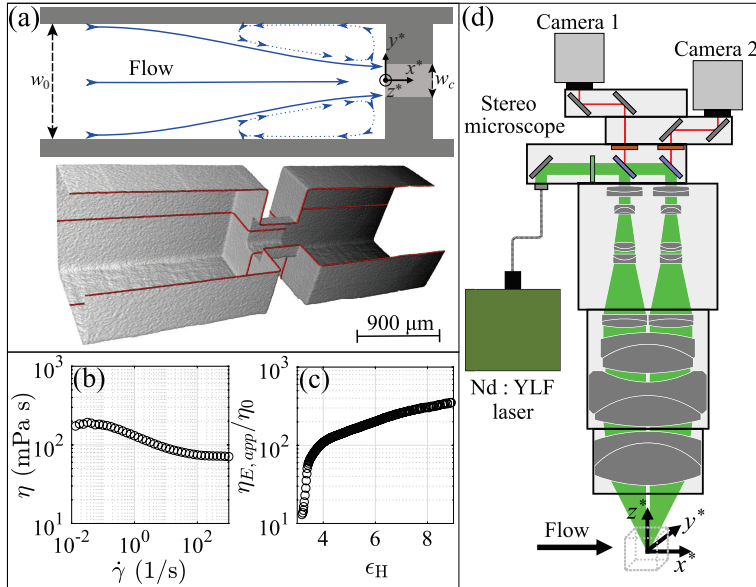


Figure 1: (a) A sketch and micro-CT scan of the glass square-sectioned contraction-expansion channel. (b, c) Shear and extensional rheology of the polyacrylamide test solution. (d) A diagram of the microtomographic PIV apparatus.

contraction geometry and fluid rheology. Indeed, for certain contraction ratios ($\beta = w_0/w_c$, the length scale ratio of uniform channel w_0 to the contraction width w_c) a lip vortex may form for $Wi < Wi_c$ (Giesekus (1968)), as summarized by Rothstein & McKinley (2001). Rothstein & McKinley (2001) also showed that the appearance of lip vortices in contraction flow is accompanied by a greater contribution of shear flow compared to extension-dominated flow where corner vortices manifest. More recently, viscoelastic contraction flow has received attention at the microscale, whereby inertia can be neglected and elastic effects are dominant (see the thorough review provided by Rodd *et al.* (2007)). For the negligible Re regime, there is an apparent void of knowledge regarding three-dimensional (3D) flow at moderate to high Wi . Due to the difficulty of resolving 3D flows at the microscale, and the immense computational burden of solving a transient 3D elastic flow numerically, this flow type has not been fully detailed either experimentally or numerically.

To date, elastic contraction flow has been studied primarily via localized or planar measurements such as particle image velocimetry (PIV), laser doppler velocimetry (LDV), or streak imagery. Global pressure measurements have also been employed to provide insights into drag reduction. In recent years, tomographic PIV (TPIV) has received increasing attention as a method whereby 3D flow volumes can be resolved via the reconstruction of a particle-laden flow from overlapping lines of sight, followed by cross-correlation between subsequent particle volumes (Elsinga *et al.* (2006a)). This method can also be applied at the microscale (μ -TPIV), with multiple lines of sight provided by stereomicroscopy. Holographic PIV (HPIV) has also shown success in taking volumetric viscoelastic flow measurements in microscale geometries (Qin *et al.* (2019, 2020)), reporting a bistable negative wake ahead of a cylinder and out-of-plane instability modes along the flow separatrix of a cross-channel. However, HPIV is quite limited in terms of volume depth and reconstruction resolution compared to μ -TPIV (Schäfer & Schröder (2011)). Nonetheless, the novel results from Qin *et al.* (2019, 2020) suggest that, despite decades of research on fundamental viscoelastic flows, deep insights are still yet to be elucidated once out-of-plane dynamics are captured.

Here, using a dilute solution of a high molecular weight polymer, we report the first investigations of 3D viscoelastic contraction flow at the microscale using the μ -TPIV method. We focus on the range of Wi encompassing the transition from the vortex growth regime (which is accompanied by the growth of a steady central jet) to the onset of periodic vortex procession (which is accompanied by the circulation of the jet). We demonstrate that the circulation of the jet has phase-wise asymmetry dependence on the nominal Wi . By fully resolving the 3D velocity field, we can assess the true velocity gradient tensor and thus the rate-of-strain tensor. We show that the procession of the corner vortex is driven by the central jet continuously retreating from regions of increased rate-of-strain, and hypothesize that the underlying driving mechanism is localized strain-hardening of the polymer solution.

2. Experimental set-up

2.1. Flow cell and viscoelastic fluid

The experiments were conducted in a square-sectioned contraction-expansion flow cell (figure 1(a)) fabricated from fused-silica glass via selective laser-induced etching (Gottmann *et al.* (2012)) using a commercial LightFab 3D printer (LightFab GmbH). This process can resolve features on the micron scale, with a surface r.m.s. of approximately 1 μm (Pimenta *et al.* (2020)). We measured the channel width and height from an x-ray microtomography scan (figure 1(a)) as $w_0 = 860 \pm 10 \mu\text{m}$ outside the contraction, and $w_c = 255 \pm 5 \mu\text{m}$ inside the contraction, yielding a contraction ratio $\beta = 3.4$. Figure 1(a) displays our dimensionless coordinate system, where each component is reduced by $w_c/2$ (e.g., $x^* = 2x/w_c$). Flow was stepped to each velocity by two syringe pumps in a push-pull configuration.

The viscoelastic test fluid was a polymeric solution composed of 107 parts-per-million (ppm) partially hydrolyzed polyacrylamide (HPAA, $M_W = 18 \text{ MDa}$, Polysciences Inc., U.S.A.), in a solvent of 85 wt% glycerol and 15 wt% deionized water. The refractive index of the fluid is closely matched to that of the fused-silica flow cell. An Anton-Paar MCR 502 stress-controlled rheometer was used with a cone and plate geometry (50 mm diameter, 1° angle) to characterize the shear viscosity of the fluid under steady shear. Figure 1(b) shows that the fluid is weakly shear thinning and has a zero shear viscosity of $\eta_0 = 184 \text{ mPa}\cdot\text{s}$. The relaxation time of the fluid was measured as $\lambda = 0.65 \text{ s}$ using a capillary breakup extensional rheometer (Haake CaBER, Thermo Fisher Scientific, see Anna & McKinley (2001)) fitted with $d_0 = 6 \text{ mm}$ diameter endplates. We plot the ratio of the apparent extensional viscosity $\eta_{E,app}$ to the zero shear viscosity η_0 , against the accumulated Hencky strain $\epsilon_H = 2\ln(d_0/d(t))$ in figure 1(c). The fluid exhibits strong strain-hardening with $\eta_{E,app} \approx 400\eta_0$ at high strains. The zero shear viscosity η_0 and the characteristic length scale $w_c/2$ are used to calculate $Re = \rho u_c w_c / 2\eta_0$ and $Wi = 2\lambda u_c / w_c$. In the present work, $Re \lesssim 10^{-2}$ and as such is considered negligible.

2.2. Microtomographic PIV (μ -TPIV)

Volumetric flow measurement can be achieved by the TPIV method, which is termed μ -TPIV when conducted via stereomicroscopy. As implemented in a LaVision FlowMaster system (LaVision GmbH), μ -TPIV uses a stereomicroscope (SteREO V20, Zeiss AG, Germany) with dual high speed cameras (Phantom VEO 410, 1280 x 800 pixels) imaging a fluid volume illuminated by a coaxial Nd:YLF laser (dual-pulsed, 527 nm wavelength), see figure 1(d). The fluid was seeded with $2\mu\text{m}$ diameter fluorescent particles (PS-FluoRed, Microparticles GmbH, Germany) to a visual concentration of 0.04 particles-per-pixel.

The flow was recorded as double-frame images captured at 12 Hz, with a flow-rate

dependent time interval between laser pulses Δt such that no particle moved more than 8 pixels. Frames were pre-processed with local background subtraction and Gaussian smoothing at 3×3 pixels. 3D calibration was performed by capturing reference images of a micro-grid at the planes $z = \pm 450 \mu\text{m}$ and $z = 0 \mu\text{m}$, fully encompassing the depth of the flow cell (w_0), and a coordinate system was interpolated between these planes using a third-order polynomial. Particle positions in 3D were reconstructed from the images using four iterations of the Fast MART (Multiplicative Algebraic Reconstruction Technique) algorithm implemented in the commercial PIV software DaVis 10.1.2 (Lavisision GmbH). Fast MART initializes the particle volume using the multiplicative line-of-sight routine (MLOS Worth & Nickels (2008); Atkinson & Soria (2009)), followed by iterations of Sequential MART (SMART Atkinson & Soria (2009)). We concluded the algorithm with five iterations of the Motion Tracking Enhancement (MTE) method (Novara *et al.* (2010); Lynch & Scarano (2015)) to reduce spurious "ghost" particles which arise from randomly overlapping lines of sight (Elsinga *et al.* (2006b)), and thus do not correlate in time. Volume self-calibration (Wieneke (2008)) was employed to improve the accuracy of reconstruction. Particle displacements between particle volumes were obtained using a multi-grid iterative cross-correlation technique, with the final pass at $32 \times 32 \times 32$ voxels with 75% overlap for a vector grid of $31 \mu\text{m}$. To reduce measurement noise the vector field was spatiotemporally filtered with a second-order polynomial regression across neighborhoods of 5^3 vectors in space and extended through five increments in time for a total kernel size of 5^4 points. This polynomial regression visibly reduced measurement noise while predominantly preserving space-time resolution owing to the small kernel size: the filtering wavelength is substantially smaller than the flow dynamics reported in this work. This is a common approach to denoise TPIV data (Scarano & Poelma (2009); Elsinga *et al.* (2010); Schneiders *et al.* (2017)). Ultimately we resolved 1600 flow volumes per recording: a duration of 133 s (200 λ).

Uncertainty quantification for TPIV is a topic of ongoing research (Atkinson *et al.* (2011); Sciacchitano (2019)), but *a priori* comparisons of experimental velocity fields to direct numerical solutions or synthetic reconstructions have yielded a TPIV uncertainty on the order of 0.1–0.3 pixels (Atkinson *et al.* (2011)). As an *a posteriori* assessment of our measurement quality, we validated conservation of mass for time-averaged flow volumes (Zhang *et al.* (1997)). Flow divergence $\nabla \cdot \mathbf{u}$ was calculated at each vector, and the error assessed relative to an assumption of incompressible flow (relative error $\zeta = (\nabla \cdot \mathbf{u})^2 / \text{tr}(\nabla \mathbf{u} \cdot \nabla \mathbf{u})$). The value ζ averaged 0.25 for $3 \leq Wi \leq 87$. Divergence error relative to the magnitude of vorticity was 0.14 at $Wi = 87$, in good agreement with a value of 0.2 from a three-camera TPIV experiment by Kempaiah *et al.* (2020).

3. Results and discussion

Measurements were taken over a range of flow velocities encompassing $3 \leq Wi \leq 87$ for a region of interest upstream of the contraction. Note that the downstream (expansion) side was imaged in a separate series of experiments, but flow remained steady across the Wi range investigated. Throughout the discussion of the flow field kinematics we nondimensionalize lengths by $w_c/2$ and velocities by U_c (the average flow velocity in the contraction). Deformation rates are hence reduced by $2U_c/w_c$. Times are nondimensionalized either by the fluid relaxation time λ or by the fundamental period of circulation in the case of periodic flows. All nondimensional quantities are indicated by a superscript ‘*’.

3.1. Steady flow at low Wi

As flow approaches the contraction at $Wi \leq 5$, a steady separation point forms where the flow separates from the walls of the channel and the flow passes as central jet through the

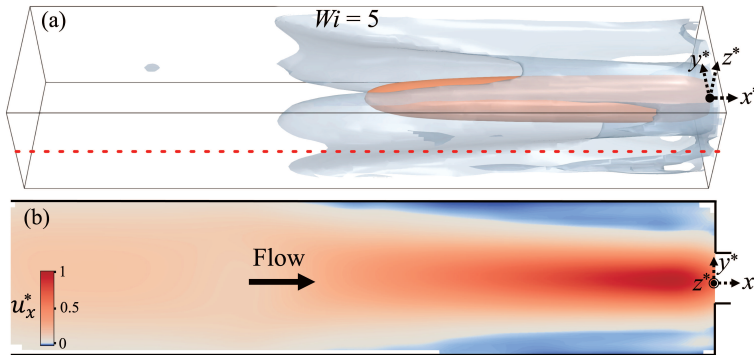


Figure 2: Averaged (a) isosurfaces and (b) midplane x^*-y^* slice of the streamwise velocity u_x^* at $Wi = 5$. The isosurfaces in (a) are pink for $u_x^* = 1/3$, and grey for $u_x^* = 0$. The dashed red line in (a) marks the u_x^* extraction used in figure 3.

constriction. Figure 2 presents (a) average isosurfaces and (b) a midplane x^*-y^* slice of the streamwise velocity u_x^* for $Wi = 5$. The pink isosurface shows $u_x^* = 1/3$ (i.e., the central jet), while the grey surface marks $u_x^* = 0$ (i.e., the edges of the recirculating regions). Flow separation follows the upstream downzero crossing of u_x^* ; the central jet is characterized by positive u_x^* , while the corner vortices drive negative u_x^* backflow along the walls towards the separation point. We did not observe any lip vortices here, which agrees with indications from the literature whereby lip vortices are unlikely for abrupt contractions with $\beta > 2$ (Rothstein & McKinley (2001)), signaling that extensional flow is dominant over shear flow.

3.2. The onset of periodic instability

For increasing Wi , the corner vortex propagates upstream but remains steady, until, for $Wi > Wi_p$, the flow transitions to a periodic instability characterised by axial fluctuation of the upstream separation point and a circumferential procession of the central jet (see movie 1 in the supplemental material for animations of the jet for $5 \leq Wi \leq 44$). Figure 3(a-e) present space-time diagrams depicting the streamwise flow velocity $u_x^*(x^*)$ along the line $(y^*, z^*) = (-w_0/w_c, 0)$ (dashed red line in figure 2(a)) for five representative values of $3 \leq Wi \leq 87$. The dimensionless vortex length L_v^* is determined by the zero-crossing of u_x^* (as indicated on figure 3(a)). The average value of L_v^* ($L_{v,avg}^*$) and the range of oscillation between $L_{v,max}^*$ and $L_{v,min}^*$ are plotted as a function of Wi in figure 3(f), indicating a transition from steady vortex growth at lower Wi to a regime of oscillation whereby L_v^* apparently no longer scales directly with Wi . The inset of figure 3(f) shows the period of oscillation ($T^* = T/\lambda$) determined by FFT of the $L_v^*(t)$ signals. Above the critical value $5 < Wi_p \leq 11$ for the onset of oscillation, the range of oscillation reaches a local maximum by $Wi = 16$, and the mean separation point actually moves downstream (i.e., L_v^* reduces) for $22 \leq Wi \leq 44$. Interestingly, the reduction in L_v^* does not affect the frequency of the instability, with the period of oscillation continuously decreasing from $T^* = 26$ at $Wi = 11$ to $T^* = 7$ at $Wi = 44$ (figure 3(f)). Our results expand on prior experimental observations made in axisymmetric abrupt contractions which saw the vortex size increase monotonically for increasing Wi , although at a lower Wi range than probed here due to larger length scales involved (e.g., $Wi < 5$ for McKinley *et al.* (1991) and $Wi < 8$, for Rothstein & McKinley (1999)). In planar microfluidic contraction flow experiments, Rodd *et al.* (2007) reported a decrease in L_v^* for a single data point at the maximum $Wi = 24$ achieved, but were unable to extrapolate the trend. Numerical work by Comminal *et al.* (2016) observed an L_v^* plateau

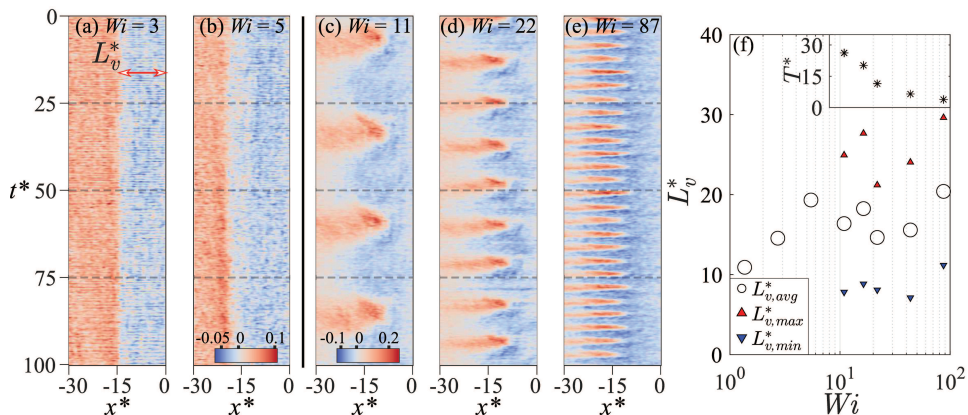


Figure 3: (a-e) Space-time diagrams of the streamwise velocity u_x^* (indicated by the colour bars) along the wall at the x^*-y^* midplane (represented as a dashed line in figure 2(a)). (f) The mean and range of values of L_v^* , with the fundamental period T^* in the insert.

accompanied by periodic vortex annihilation for $Wi > 14$ in a 2D contraction, which they attributed to an accumulation of elastic strain upstream of the contraction. However, they acknowledged that their use of the Oldroyd-B constitutive model (Oldroyd (1950)) lacks physical mechanisms (such as finite-extensibility) which would otherwise limit elastic stress.

3.3. Out of plane jet dynamics

As shown in the x^*-t^* space-time diagrams in figure 3(a-e), the flow instability is strongly periodic for $Wi \geq 11$. Thus, to collapse the dataset and further reduce noise we deploy time synchronous averaging (TSA) to reduce the time dimension into a single average cycle. This method is further discussed in Bechhoefer & Kingsley (2009). We isolated the time series of velocity magnitude at a single point in the volume, then used the local maxima in the time series at that point to segregate each period at all points in the volume. The cycles are mapped to a normalized phase time ϕ^* ranging from 0 to 1 (i.e., 1 cycle), and averaged into $f_s T$ bins where f_s is the sampling frequency (12 Hz) and $T = T^*/\lambda$ is the average period (T^* shown in figure 3(f)). Henceforth, phase averaged quantities will be marked by $\langle \cdot \rangle$.

We used the phase-binned data to investigate the 3D trajectory of the central jet passing through the toroidal corner vortex. We found the maximum flow velocity in each y^*-z^* plane along the x^* axis for $-L_v^* \leq x^* \leq 0$. Thus, we extract $x^*-y^*-z^*$ trajectories of the circulating inner jet as it approaches the contraction. To quantify fluctuations in the jet velocity throughout phase time, we calculate the normalized fluctuating velocity along x^* as $\langle \hat{U} \rangle(\phi^*) = (1/n_{x^*}) \sum_{x^*=-L_v^*}^{x^*=0} (\langle U \rangle^*(x^*, \phi^*) - \langle \bar{U} \rangle^*(x^*)) / \langle U \rangle^*(x^*)_{max}$. In this way $\langle \hat{U} \rangle$ is not affected by the accelerating flow velocity as the jet approaches the contraction. Data of $\langle \hat{U} \rangle$ are presented in figure 4(a) for $Wi \geq 5$, along with snapshots of the location of the jet in figure 4(b, c) for $Wi = 44$ and $Wi = 87$. We observe a phase-wise asymmetry of the jet in both the fluctuating component of velocity and the jet location. For each Wi , the jet starts at the same place in the channel at $\phi^* = 0$, but with an opposite directionality about x^* for $Wi < 16$ (the direction of circulation is seemingly random between experiments). Maxima and minima in $\langle \hat{U} \rangle$ are evident for $Wi = 11$ near $\phi^* = 0.18, 0.88$ and 0.56 , respectively, and apparent but slightly degraded by $Wi = 22$. The fact that the velocity fluctuation is small ($< 5\%$) and almost symmetric about $\phi^* = 0.5$ indicates that the cyclical fluctuation in the $11 \leq Wi \leq 22$ regime is likely geometric in origin as the channel has an $\approx 5 \mu\text{m}$ (or $\approx 0.02w_c$) variation between the width and height. At higher Wi (e.g., $Wi = 44$ and $Wi = 87$), the jet had the

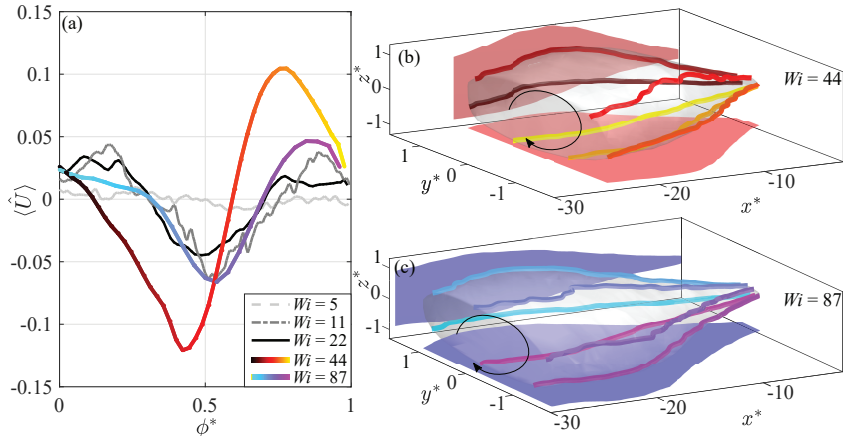


Figure 4: (a) The axially-averaged fluctuating velocity of the jet over phase time ϕ^* . (b, c) Trajectories (coloured by ϕ^* in (a)) and planar projections of the jet at $Wi = 44$ and 87 .

same directionality as for $Wi = 22$ and was mapped to the same locations in phase time, but strikingly the dual $\langle \hat{U} \rangle$ peaks are eliminated. Instead, we observe a single minimum and maximum for $\langle \hat{U} \rangle$ and the values occur at different phase times from those seen at lower velocities. Thus it is inferred that the peak fluctuation is independent of the y^* - z^* coordinate between different Wi . To relate velocity fluctuations within the jet to the spatial distribution, we present in figure 4(b, c) trajectories of the jet core position in x^* - y^* - z^* over phase time. Here we see the minimum $\langle \hat{U} \rangle$ for $Wi = 44$ coincides with a skewed curvature of the jet towards $+z^*$ near $\phi^* = 0.42$, and the jet is comparatively tighter towards $z^* = 0$ which aligns in time with the maximum $\langle \hat{U} \rangle$ near $\phi^* = 0.78$: the distribution of the jet varies inversely with the fluctuating velocity such that flow rate is preserved. A similar effect is seen for $Wi = 87$, but with a shifted phase timing of $\langle \hat{U} \rangle$, placing the asymmetry more in the x^* - y^* plane. Reconfiguration to single-sided asymmetry in the jet at $Wi \geq 44$ coincides with a phenomenon previously discussed: the growth plateau in L_v^* from $11 \leq Wi \leq 22$ despite a decreasing core period of the circulating jet (figure 3(f)). Whereas the symmetrically swirling jet appears to prohibit vortex growth, a break to strong asymmetry above $Wi = 22$ proves a preferable route and L_v^* again increases for increasing Wi .

3.4. The role of the rate-of-strain tensor

Dilute solutions of high molecular weight polymers are known to shear-thin under shear flow, and strain-harden under extensional deformations (Tirtaatmadja & Sridhar (1993); Solomon & Muller (1996)), as we observed for the HPA fluid used in our work (figure 1(b, c)). Furthermore, as summarized in Rothstein & McKinley (2001), the lack of lip vortices observed in our experiments implies that extensional flow is dominant over shear flow. We can gain qualitative insight into the relevance of strain-hardening on the dynamics of our micro-contraction flow by considering the local rate-of-strain tensor $\mathbf{D} = (\nabla \langle \mathbf{u} \rangle + \nabla \langle \mathbf{u} \rangle^\top) / 2$. Here we rely solely on the μ -TPIV measurements to obtain the velocity vector field before calculating \mathbf{D} . We take the magnitude of \mathbf{D} as $\langle \dot{\gamma} \rangle = \sqrt{2(\mathbf{D} : \mathbf{D})}$ (reduced as $\langle \dot{\gamma} \rangle^* = \langle \dot{\gamma} \rangle w_c / (2U_c)$) to highlight regions of high rate-of-strain where strain-hardening of the HPA is more likely. We extracted y^* - z^* slices at an arbitrary $x^* = -8$ for $Wi = 87$ to show a simplified perspective on relationship between $0.5 \langle \dot{\gamma} \rangle^*$ and the location of the jet (coloured contours of $0.5 \langle U \rangle^*$, $\langle U \rangle^* = \langle U \rangle / U_c$) in figure 5(a-d). The subplots progress along phase time ϕ^* , with each plane including the $0.5 \langle U \rangle^*$ contour from the following phase time. Two trends are noted: first that

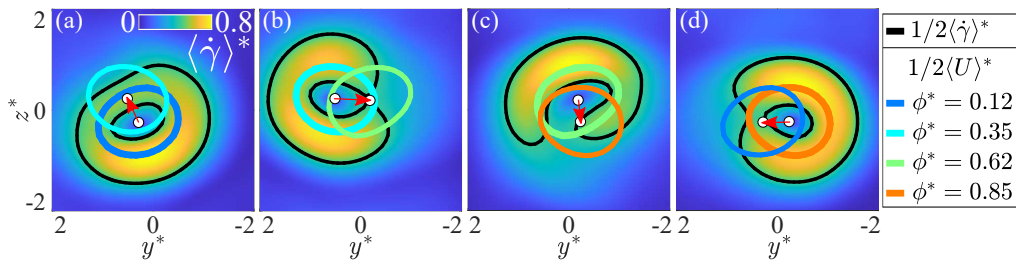


Figure 5: y^*-z^* slices of $\langle \dot{\gamma} \rangle^*$ at $x^* = -8$, with black contours of $0.5\langle \dot{\gamma} \rangle^*$ and coloured contours of $0.5\langle \dot{U} \rangle^*$ for $Wi = 87$, for increasing normalized phase time ϕ^* .

while the jet (the solid coloured contour) stays centered about $\langle \dot{\gamma} \rangle^*$, the jet location forward in time is always towards the exterior of the $\langle \dot{\gamma} \rangle^*$ contour. Secondly, a phase-wise asymmetry manifests in the distribution of $\langle \dot{\gamma} \rangle^*$. $\phi^* = 0.12$ has low asymmetry in $\langle \dot{U} \rangle^*$ (figure 5(b)), as well as in the distribution of $\langle \dot{\gamma} \rangle^*$. By $\phi^* = 0.62$, $\langle \dot{U} \rangle^*$ is highly deviated and this aligns with a strong mismatch in $\langle \dot{\gamma} \rangle^*$ about the circumference of the jet. Therefore, it appears that a mismatch in rate-of-strain about the jet can strongly influence the phase-wise progression of the jet as it circulates, with positive and negative fluctuations in $\langle \dot{U} \rangle^*$ accompanied by an unbalanced distribution of $\langle \dot{\gamma} \rangle^*$.

In figure 6, we present isosurfaces of $0.5\langle \dot{\gamma} \rangle^*$ and $0.5\langle \dot{U} \rangle^*$, the maximum rate-of-strain and flow velocity, for $Wi = 87$. Figure 6(a-d) show 4 timesteps throughout a circulation, where the volume of high rate-of-strain forms a band about the circumference of the core of the jet (the pink isosurface). Moreover, the $\langle \dot{\gamma} \rangle^*$ isosurface extends further upstream on one side of the jet for all timesteps, i.e., the rate-of-strain is greater along one side of the jet. An animated loop of the jet circulating with the rate-of-strain volume is shown in supplemental movie 2.

We directly compare the rate-of-strain forward in time in figure 6(e) as projections of $\langle \dot{\gamma} \rangle^*$ from (a-d) from the $-x^*$ direction. Moving clockwise from the $\phi^* = 0.12$ isosurface, each surface forward in time presents a decrease in the rate-of-strain in the clockwise direction. In other words, a perpetual retreat of the central jet from regions of increased rate-of-strain. The dynamics of elastic contraction flow has been reported to be sensitive to the extensional rheology (Rothstein & McKinley (2001)), and since our HPA solution strain-hardens (figure 1(c)), we can infer from the flow kinematics that the central jet moves about the contraction driven by gradients of strain-hardening HPA, which will tend to follow the regions of increased rate-of-strain. This sheds new light onto the likely significance of extensional rheology for *local* dynamics in viscoelastic contraction flow, as experimentally describing flow topology via directly resolving the rate-of-strain tensor has not been achieved hitherto for elastic flow instability.

4. Conclusions

Using μ -TPIV, we have experimentally resolved for the first time the highly 3D dynamics of viscoelastic flow through a square-square micro-contraction at low Re and high Wi . We captured steady and periodic flow instability for a central jet of fluid passing through a toroidal vortex pinned about the contraction entrance, and observed a new vortex growth plateau whereby the period of instability decreases with Wi but the enveloped vortex volume stagnates. For low $11 \leq Wi \leq 22$, the jet circulates with a symmetric cyclical velocity fluctuation likely originating from geometric imperfections. This region coincides with the vortex growth plateau. At higher $Wi \geq 44$, a strong asymmetry in the jet forms which

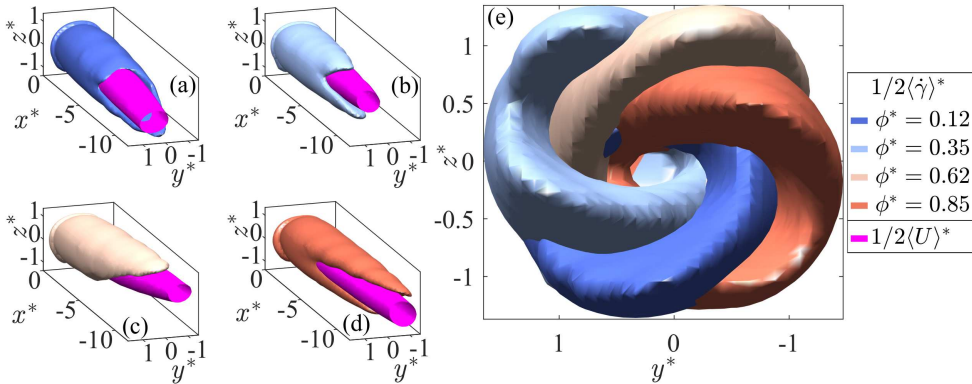


Figure 6: (a-d) Phase-averaged isosurfaces of $0.5\langle\dot{\gamma}\rangle^*$ and $0.5\langle U\rangle^*$ for $Wi = 87$. (e) The $-x^*$ projection of the $\langle\dot{\gamma}\rangle^*$ surfaces from (a-d), coloured by their normalized phase time ϕ^* . For advancing time ϕ^* , the inner jet displaces towards decreasing rate-of-strain.

corresponds to exiting the growth plateau. This would indicate that the asymmetric mode provides a preferable route to vortex growth. We determined the first experimental mapping of the full rate-of-strain tensor to transient dynamics for viscoelastic flow instabilities. We relate regions of increased rate-of-strain and the extensional rheology of the fluid to the directionality of the circulating jet. Gradients of strain-hardening in the fluid provide a likely circulation mechanism as the jet retreats from locally strain hardened regions of the flowing viscoelastic polymer solution: a new insight on the significance of extensional rheology to local dynamics of viscoelastic contraction flow.

Funding. D.W.C., A.Q.S. and S.J.H. acknowledge financial support from the Japanese Society for the Promotion of Science (JSPS, Grant Nos. 21K14080, 18K03958, 18H01135, and 21K03884).

Declaration of interests. The authors report no conflict of interest.

REFERENCES

- AFONSO, A.M., OLIVEIRA, P.J., PINHO, F.T. & ALVES, M.A. 2011 Dynamics of high-Deborah-number entry flows: a numerical study. *Journal of Fluid Mechanics* **677**, 272.
- ANNA, S.L. & MCKINLEY, G.H. 2001 Elasto-capillary thinning and breakup of model elastic liquids. *Journal of Rheology* **45** (1), 115–138.
- ATKINSON, C., COUDERT, S., FOUCAUT, J-M, STANISLAS, M. & SORIA, J. 2011 The accuracy of tomographic particle image velocimetry for measurements of a turbulent boundary layer. *Experiments in Fluids* **50** (4), 1031–1056.
- ATKINSON, C. & SORIA, J. 2009 An efficient simultaneous reconstruction technique for tomographic particle image velocimetry. *Experiments in Fluids* **47** (4-5), 553.
- BECHHOEFER, E. & KINGSLEY, M. 2009 A review of time synchronous average algorithms. In *Annual Conference of the Prognostics and Health Management Society*, , vol. 23, pp. 1–10.
- BOGER, D.V. 1987 Viscoelastic flows through contractions. *Annual Review of Fluid Mechanics* **19** (1), 157–182.
- COMMINAL, R., HATTEL, J.H., ALVES, M.A. & SPANGENBERG, J. 2016 Vortex behavior of the Oldroyd-B fluid in the 4-1 planar contraction simulated with the streamfunction–log-conformation formulation. *Journal of Non-Newtonian Fluid Mechanics* **237**, 1–15.
- ELSINGA, G.E., ADRIAN, R.J., VAN OUDHEUSDEN, B.W. & SCARANO, F. 2010 Three-dimensional vortex organization in a high-Reynolds-number supersonic turbulent boundary layer. *Journal of Fluid Mechanics* **644**, 35–60.
- ELSINGA, G.E., SCARANO, F., WIENEKE, B. & VAN OUDHEUSDEN, B.W. 2006a Tomographic particle image velocimetry. *Experiments in Fluids* **41** (6), 933–947.
- ELSINGA, G.E., VAN OUDHEUSDEN, B.W. & SCARANO, F. 2006b Experimental assessment of tomographic-

- PIV accuracy. In *13th international symposium on applications of laser techniques to fluid mechanics, Lisbon, Portugal*, vol. 20.
- GIESEKUS, H.W. 1968 Non-linear effects in the flow of visco-elastic fluids through slits and holes. *Rheological Acta* **7**, 127–138.
- GOTTMANN, J., HERMANS, M. & ORTMANN, J. 2012 Digital photonic production of micro structures in glass by in-volume selective laser-induced etching using a high speed micro scanner. *Physics Procedia* **39**, 534–541.
- KEMPAIAH, K.U., SCARANO, F., ELSINGA, G.E., VAN OUDHEUSDEN, B.W. & BERMEL, L. 2020 3-dimensional particle image velocimetry based evaluation of turbulent skin-friction reduction by spanwise wall oscillation. *Physics of Fluids* **32** (8), 085111.
- LYNCH, K.P. & SCARANO, F. 2015 An efficient and accurate approach to MTE-MART for time-resolved tomographic PIV. *Experiments in Fluids* **56** (3), 66.
- McKINLEY, G.H., RAIFORD, W.P., BROWN, R.A. & ARMSTRONG, R.C. 1991 Nonlinear dynamics of viscoelastic flow in axisymmetric abrupt contractions. *Journal of Fluid Mechanics* **223**, 411–456.
- NOVARA, M., BATENBURG, K.J. & SCARANO, F. 2010 Motion tracking-enhanced MART for tomographic PIV. *Measurement Science and Technology* **21** (3), 035401.
- OLDROYD, J.G. 1950 On the formulation of rheological equations of state. *Proceedings of the Royal Society of London. Series A. Mathematical and Physical Sciences* **200** (1063), 523–541.
- PIMENTA, F. & ALVES, M.A. 2017 Stabilization of an open-source finite-volume solver for viscoelastic fluid flows. *Journal of Non-Newtonian Fluid Mechanics* **239**, 85–104.
- PIMENTA, F., TODA-PETERS, K., SHEN, A.Q., ALVES, M.A. & HAWARD, S.J. 2020 Viscous flow through microfabricated axisymmetric contraction/expansion geometries. *Experiments in Fluids* **61** (9), 1–16.
- QIN, B., RAN, R., SALIPANTE, P.F., HUDSON, S. & ARRATIA, P.E. 2020 Three-dimensional structures and symmetry breaking in viscoelastic cross-channel flow. *Soft Matter* **16** (30), 6969–6974.
- QIN, B., SALIPANTE, P.F., HUDSON, S.D. & ARRATIA, P.E. 2019 Upstream vortex and elastic wave in the viscoelastic flow around a confined cylinder. *Journal of Fluid Mechanics* **864**.
- RODD, L.E., COOPER-WHITE, J.J., BOGER, D.V. & McKINLEY, G.H. 2007 Role of the elasticity number in the entry flow of dilute polymer solutions in micro-fabricated contraction geometries. *Journal of Non-Newtonian Fluid Mechanics* **143** (2-3), 170–191.
- ROTHSTEIN, J.P. & McKINLEY, G.H. 1999 Extensional flow of a polystyrene Boger fluid through a 4: 1: 4 axisymmetric contraction/expansion. *Journal of Non-Newtonian Fluid Mechanics* **86** (1-2), 61–88.
- ROTHSTEIN, J.P. & McKINLEY, G.H. 2001 The axisymmetric contraction–expansion: the role of extensional rheology on vortex growth dynamics and the enhanced pressure drop. *Journal of Non-Newtonian Fluid Mechanics* **98** (1), 33–63.
- SCARANO, F. & POELMA, C. 2009 Three-dimensional vorticity patterns of cylinder wakes. *Experiments in Fluids* **47** (1), 69–83.
- SCHÄFER, L. & SCHRÖDER, W. 2011 Comparison of holographic and tomographic particle-image velocimetry turbulent channel flow measurements. In *Journal of Physics: Conference Series*, vol. 318, p. 022019. IOP Publishing.
- SCHNEIDERS, J.F.G., SCARANO, F. & ELSINGA, G.E. 2017 Resolving vorticity and dissipation in a turbulent boundary layer by tomographic PTV and VIC+. *Experiments in Fluids* **58** (4), 27.
- SCIACCHITANO, A. 2019 Uncertainty quantification in particle image velocimetry. *Measurement Science and Technology* **30** (9), 092001.
- SOLOMON, M.J. & MULLER, S.J. 1996 The transient extensional behavior of polystyrene-based Boger fluids of varying solvent quality and molecular weight. *Journal of Rheology* **40** (5), 837–856.
- TIRTAATMADJA, V. & SRIDHAR, T. 1993 A filament stretching device for measurement of extensional viscosity. *Journal of Rheology* **37** (6), 1081–1102.
- WHITE, S.A., GOTSIS, A.D. & BAIRD, D.G. 1987 Review of the entry flow problem: experimental and numerical. *Journal of Non-Newtonian Fluid Mechanics* **24** (2), 121–160.
- WIENEKE, B. 2008 Volume self-calibration for 3D particle image velocimetry. *Experiments in Fluids* **45** (4), 549–556.
- WORTH, N.A. & NICKELS, T.B. 2008 Acceleration of tomo-PIV by estimating the initial volume intensity distribution. *Experiments in Fluids* **45** (5), 847–856.
- ZHANG, J., TAO, B. & KATZ, J. 1997 Turbulent flow measurement in a square duct with hybrid holographic PIV. *Experiments in Fluids* **23** (5), 373–381.